

1 **Title: Single-cell analysis identifies NOTCH3-mediated interactions between stromal cells that**
 2 **promote microenvironment remodeling and invasion in lung adenocarcinoma**

3 Handan Xiang^{1, #, *}, Yidan Pan^{2, #}, Marc A. Sze², Marta Wlodarska³, Ling Li⁴, Karyn Ann Van De Mark¹,
 4 Haleema Qamar¹, Casey J. Moure³, Douglas E. Linn⁵, Josephine Hai^{5, 8}, Ying Huo⁵, James Clarke², Tze Guan
 5 Tan⁶, Samantha Ho⁶, Karen W. Teng⁶, Muhammad N. Ramli⁴, Michael Nebozhyn², Chunsheng Zhang²,
 6 Julianne Barlow⁷, Corinne E. Gustafson⁷, Savanna Gornisiewicz⁷, Thomas P. Albertson⁷, Stephanie L.
 7 Korle⁷, Raphael Bueno⁷, Lily Y. Moy⁵, Elisabeth H. Vollmann¹, Derek Y. Chiang^{2, 9}, Philip E. Brandish^{3, 10},
 8 Andrey Loboda^{2, *}

9 ¹Discovery Immunology, Merck & Co., Inc., Cambridge, MA, USA

10 ²Data and Genome Sciences, Merck & Co., Inc., Boston, MA, USA

11 ³Discovery Oncology, Merck & Co., Inc., Boston, MA, USA

12 ⁴Quantitative Bioscience, MSD, Singapore

13 ⁵Quantitative Bioscience, Merck & Co., Inc., Boston, MA, USA

14 ⁶Discovery Cardiometabolic Diseases, MSD, Singapore

15 ⁷The Division of Thoracic Surgery, Brigham & Women's Hospital, Harvard Medical School, Boston, MA,
 16 USA

17 ⁸ Current address: Solid Tumor Translational Medicine, Bristol Myers Squibb, Cambridge, MA, USA

18 ⁹ Current address: Translational Sciences Oncology, Bayer US LLC, Cambridge, MA, USA

19 ¹⁰ Current address: Bicycle Therapeutics, Cambridge, MA, USA

20 # Equal contribution

21 * To whom correspondence should be addressed: 1) Handan Xiang; 320 Bent St, Cambridge, MA, USA
 22 02141; Tel: +1-617-992-3151, email: handan.xiang@merck.com; 2) Andrey Loboda; 33 Avenue Louis
 23 Pasteur, Boston, MA, USA 02115; Tel: +1-617-992-2490, email: andrey_loboda@merck.com
 24

25 **Running Title**

26 Altered NOTCH3 signaling in LUAD stromal cells
 27

28 **Disclosure of Potential Conflicts of Interest**

29
 30 The authors declare the following competing financial interest(s): HX, MAS, KAVDM, DL, JC, TGT, SH,
 31 TWWK, MNR, MN, CZ, LYM, EV, and AL are employees of Merck Sharp & Dohme LLC, a subsidiary of
 32 Merck & Co., Inc., Rahway, NJ, USA, and own stock in Merck & Co., Inc., Rahway, NJ, USA. Dr. Raphael
 33 Bueno is funded by the NCI, NHLBI, NIBIB and has received research grants from Merck, Genentech,
 34 Roche, Serum, and Bayer. He also has equity in the device company, Navigation Sciences. JH is an
 35 employee of, and owns stock in, Bristol Myers Squibb. DYC is an employee of, and owns stock options in,
 36 Bayer. PEB is an employee, and owns stock options, in Bicycle Therapeutics. All other authors declare no
 37 potential conflicts of interest.

38 **Abstract**

39 Cancer immunotherapy has revolutionized the treatment of lung adenocarcinoma (LUAD);
40 however, a significant proportion of patients do not respond. Recent transcriptomic studies to
41 understand determinants of immunotherapy response have pinpointed stromal-mediated resistance
42 mechanisms. To gain a better understanding of stromal biology at the cellular and molecular level in
43 LUAD, we performed single-cell RNA-sequencing of 256,379 cells, including 13,857 mesenchymal cells,
44 from 9 treatment-naïve patients. Among the mesenchymal cell subsets, *FAP⁺PDPN⁺* cancer-associated
45 fibroblasts (CAFs) and *ACTA2⁺MCAM⁺* pericytes were enriched in tumors and differentiated from lung
46 resident fibroblasts. Imaging-mass cytometry revealed that both subsets were topographically adjacent
47 to the perivascular niche and had close spatial interactions with endothelial cells (ECs). Modeling of
48 ligand and receptor interactomes between mesenchymal and ECs identified that NOTCH signaling drives
49 these cell-to-cell interactions in tumors, with pericytes and CAFs as the signal receivers and arterial and
50 *PLVAP^{high}* immature neovascular ECs as the signal senders. Either pharmacologically blocking NOTCH
51 signaling or genetically depleting NOTCH3 levels in mesenchymal cells significantly reduced collagen
52 production and suppressed cell invasion. Bulk RNA-sequencing data demonstrated that *NOTCH3*
53 expression correlated with poor survival in stroma-rich patients and that a T cell-inflamed gene
54 signature only predicted survival in patients with low *NOTCH3*. Collectively, this study provides valuable
55 insights into the role of NOTCH3 in regulating tumor stroma biology, warranting further studies to
56 elucidate the clinical implications of targeting NOTCH3 signaling.

57 **Significance**

58 NOTCH3 signaling activates tumor-associated mesenchymal cells, increases collagen production, and
59 augments cell invasion in lung adenocarcinoma, suggesting its critical role in remodeling tumor stroma.

60 Introduction

61 Lung Adenocarcinoma (LUAD) is the most prevalent form of primary lung cancer in the USA,
62 accounting for 40% of all lung cancer cases(1). The treatment of advanced LUAD has undergone a
63 paradigm shift with the advent of immune checkpoint blockade (ICB), which inhibits immuno-
64 suppressive signaling pathways such as PD-1(2). However, the majority of patients either do not respond
65 or relapse(2). Transcriptomic studies using patient-derived samples have shown that the enrichment of
66 a stromal or mesenchymal gene signature is strongly associated with resistance to ICB(3,4). This
67 suggests that mesenchymal cells, including cancer-associated fibroblasts (CAFs), play a crucial role in
68 mediating immunosuppression and treatment resistance in the tumor stroma.

69 Single-cell RNA-sequencing (scRNA-seq) has revolutionized our understanding of tumor
70 mesenchymal cell and CAF biology, providing valuable insights into CAF interactions with the immune
71 system. In pancreatic cancer, which is characterized by a high degree of desmoplasia, two major CAF
72 subsets have been identified through scRNA-seq studies: "myofibroblastic CAFs" (myCAFs) with high
73 expression of alpha smooth muscle actin (α SMA or ACTA2) and extracellular matrix (ECM) molecules,
74 and "inflammatory CAFs" (iCAFs) with high levels of cytokines and chemokines(5,6). The selective
75 depletion of LRRC15+ myCAFs has been shown to enhance the efficacy of ICB in a mouse model and is
76 being explored clinically, indicating mesenchymal cells with a "myCAF" phenotype suppress tumor
77 immunity(7). In LUAD, scRNA-seq has been leveraged to study TME heterogeneity, cell-cell interactions,
78 and the immunophenotypes of tumor-infiltrating immune cells(8-10). However, previous scRNA-seq
79 studies investigating mesenchymal cell or CAF biology in LUAD have been limited in terms of the number
80 of profiled stromal cells, their relationship to previously defined "myCAF" and "iCAF" phenotypes, and
81 their ability to capture cellular spatial architecture and associated signaling pathways.

82 To overcome these limitations, we harnessed scRNA-seq and imaging mass cytometry (IMC) to
83 better decipher stromal heterogeneity and spatial localization. An in-depth investigation of the stromal
84 interplay by ligand-receptor analysis revealed the activation of the NOTCH pathway in tumor-associated
85 pericytes and CAFs driven by endothelium-derived NOTCH ligands. Leveraging publicly available patient
86 sequencing data, we illustrated the ability of NOTCH3 in combination with several ICB response
87 biomarkers to predict survival. Our study provides insights beyond previous scRNA-seq studies in
88 understanding tumor stroma biology, NOTCH driven-intercellular crosstalk, and the clinical relevance of
89 NOTCH3 as a potential stromal target.

90 **Materials and Methods**

91 **Ethics statement and study subjects.**

92 All tissue samples from 9 patients for the scRNA sequencing (cohort A) were obtained from Brigham and
93 Women's Hospital, with written informed consent from the patients. The study was conducted in
94 accordance with recognized ethical guidelines of the U.S. Common Rule and Belmont Report and was
95 approved by the Institutional Review Board (IRB) protocol DFCI #98-063. The patient samples were
96 sequenced using the OncoPanel platform(11) and the mutation status of 4 common LUAD tumor
97 suppressor and oncogenes (TP53, EGFR, K-RAS, and MET) was provided in Supplementary Table 1. LUAD
98 samples from a secondary cohort (B) of 7 patients for IMC were purchased from BioIVT, ISpecimen, and
99 Discovery Life Sciences. These samples were acquired with written informed consent from the patients
100 approved by the commercial suppliers' IRB protocols or under their partners' IRB protocols, in
101 accordance with recognized ethical guidelines of the U.S. Common Rule and Belmont Report. Please
102 refer to the Supplementary Table 1 for more details.

103 **Preparation of single-cell suspensions**

104 Tumors (T) or Adjacent Non-Tumor (ANT) tissues from cohort A were minced with scissors and digested
105 with a human tumor dissociation kit (Miltenyi Biotec, 130-095-929), as per the manufacturer's protocol
106 with some modifications. For digesting lung samples for MRC001-004, the digestion cocktail from the kit
107 was used, whereas the digestion cocktail with the addition of 0.8 mg/mL dispase II (Sigma, 4942078001)
108 was used to digest MRC006-10. In brief, each lung sample in 5mL of digestion cocktail buffer was put
109 into a gentleMACS Octo dissociator (Miltenyi Biotec) for 30 minutes to 1 hour depending on the tumor
110 size in a "*37C_h_TDK_3 digestion*" program. 20 ml of 10% FBS DMEM (ThermoFisher) media was added
111 into the digestion to stop the reaction and the material was further filtered through a 70- μ m filter
112 (Miltenyi Biotec). The remaining clumps on filters were grounded using the bottom of a 1-ml syringe
113 (BD). Cell suspensions were spun down, lysed using ACK buffer (ThermoFisher), and spun down again to
114 obtain single-cell suspensions ready for downstream experiments.

115 **Cell sorting**

116 To prepare viable cells for scRNA-seq, single-cell suspensions from MRC001-003 were stained with a
117 live/dead dye (ThermoFisher, L34975) over ice for 15 minutes in the dark. Single cells from donor
118 MRC004, 006-010 were stained with a cocktail of live/dead dye, an Fc blocker (Biolegend, 422302), and

119 an anti-CD45 antibody (BD, 560976) over ice for 30 minutes before proceeding to cell sorting. Viable
120 cells or viable CD45+/CD45- cells were sorted out using a FACS Aria III cell sorter (BD).

121 **Droplet-based single-cell sequencing**

122 Sorted viable cells were processed by Chromium Single cell 3' Reagent v3 kits (10XGenomics, 120234) to
123 generate single-cell cDNAs and prepare barcoded libraries, as per the manufacturer's protocol. Sorted
124 live cells were suspended into a cell density of around 1 million cells/mL in 0.1% BSA of PBS. To minimize
125 doublet percentages, 4000 cells for donor MRC001-003 or 6000 cells for the remaining donors were
126 loaded into each lane of a 10X chip. Cells were then partitioned into single-cell gel beads in emulsions
127 (GEMs) inside the Chromium instrument, where full-length cDNA synthesis occurred. Cleaned-up cDNAs
128 were then amplified, fragmented, and attached with 5'-adaptor and sample index. Libraries were
129 sequenced using a 150 bp paired-end configuration.

130 **Immunohistochemistry (IHC), Immunofluorescence (IF) staining, and Imaging mass cytometry (IMC)**

131 Tumor samples were fixed in 10% formalin, stored in 70% ethanol before paraffin embedding, and cut
132 into 5- μ m sections. IHC staining was performed as previously described(12). Slides were deparaffinized,
133 rehydrated, boiled with DC NxGen (Biocare Medical), incubated in Peroxidized 1 (Biocare Medical,
134 PX968), and blocked with Background Punisher (Biocare Medical, IP974G20) before staining with
135 primary antibodies: anti-TTF1 (Abcam, ab133638) and anti-P63 (Biocare Medical, CM 163A). Sections for
136 IF staining were deparaffinized, rehydrated, and boiled as described above. Sections were then stained
137 with primary antibodies: NOTCH3 (Abcam, ab23426) and MCAM (Abcam, ab210072).

138 6- μ m tissue sections from cohort B were stained with 18 antibodies (Supplementary Table 2), which
139 include markers covering mesenchymal cells (FAP, MCAM, ACTA2, CD90, and collagen I), ECs (CD31),
140 tumor/epithelial cells (E-cadherin), non-epithelial cells (Vimentin), and immune cells (CD3, CD4, CD8,
141 CD68, CD14, CD33, CD15, CD16, CD11C, and CD20). CD14, CD11C, and CD33 were removed for further
142 analysis due to poor staining quality. Hyperion Imaging System (Fluidigm) was utilized to acquire a
143 randomly selected tumor area on slides for each LUAD section. The process and analysis of IMC images
144 were followed as previously reported(13). In brief, using Fiji software, IMC mcd. Files were transformed
145 into stack tiff files, which were then imported into Ilastik (Version 1.3.2) to produce cell segmentation
146 masks followed by generation of probability masks using CellProfiler (Version 3.1.5). HistoCAT (version
147 1.75) used all files created above to produce t-SNE plots for projecting high-dimensional single-cell data
148 into two dimensions to enable visualization of marker-specific cell types as well as a Phenograph to

149 define complex phenotypes shared across tumors based on the staining intensity of tested cell markers.
150 The phenograph was used to perform neighborhood analysis with histoCAT default settings, in which a
151 permutation test to compare the number of interactions between all cell types in a given image to that
152 of a matched control containing randomized cell phenotypes was used to determine the p value.

153 **Primary cell culture**

154 Mesenchymal cells were expanded from freshly resected tumor samples obtained from MRC002, -003,
155 and -004 in cohort A, following a previously described protocol (12). The tumors were minced and
156 digested into approximately 1-mm³ fragments. These fragments were then placed in 6-well tissue
157 culture plates containing DMEM supplemented with 10% heat inactivated (HI) FBS. Mesenchymal cells
158 were allowed to extravasate from tissue fragments and were expanded until reaching confluency before
159 passaging. Cells were stained with antibodies: NOTCH3 (BD, 745463) and MCAM (Biolegend, 361004) for
160 flow cytometry analysis. These cells were used in subsequent assays within 10 passages. D4A1 cancer-
161 associated fibroblasts were purchased from Bio IVT. The cells were derived from a stage II lung
162 adenocarcinoma patient. The donor number associated with D4A1 fibroblasts is 426674A1, and the lot
163 number is DT01086P1. Human pulmonary artery ECs were purchased from Lonza and cultured in the
164 conditioned media per Lonza's instruction. NCI-H1299 cells were obtained from American Type Culture
165 Collection and cultured in F12/K and RPMI-1640 (Gibco, ThermoFisher) supplemented with 10% HI FBS.
166 The cell line was authenticated by short-tandem repeat profiling and tested negative for *Mycoplasma*.
167 NCI-H1299 cells were infected with Incucyte® Nuclight Lentivirus (Sartorius) and selected with
168 Puromycin to establish a mKate2+ stable cell line for the invasion assay. All cells were maintained at
169 37°C and 5% CO₂ in an incubator. For compound treatment, MRK-003 (Merck & Co., Inc., Rahway, NJ,
170 USA (14)), a γ -secretase inhibitor, was used.

171 **Real-time Quantitative PCR (RT-qPCR)**

172 For MRK-003 treatment, 1 x 10⁵ ECs and 1 x 10⁵ mesenchymal cells were co-cultured and seeded into
173 one well of a 6-well plate. The endothelial conditioned medium was used for the co-culture. On the next
174 day, cells were changed to fresh media containing DMSO or 1 μ M MRK-003. For siRNA transfection, 2 x
175 10⁵ ECs and 2 x 10⁵ mesenchymal cells were co-cultured in one well of a 6-well plate. On the next day,
176 200 pmol of siNOTCH3_1 (Thermo Fisher Scientific, HSS107256), siNOTCH3_2 (ThermoFisher,
177 HSS107254), or non-targeting control (siNT) was transfected into each well using Lipofectamine RNAi
178 Max (ThermoFisher). RNA and supernatants were collected 3 days after treatment for subsequent

179 analysis. RNAs were extracted using the RNeasy Plus Mini Kit (Qiagen), and 1µg of RNA was used for
180 cDNA synthesis using iScript cDNA Synthesis Kit (Bio-Rad). TaqMan™ Human Extracellular Matrix &
181 Adhesion Molecules Arrays (ThermoFisher) and following TaqMan™ primers were used: *HEYL*
182 (Hs01113778_m1), *HEY1* (Hs05047713_s1), *HES1* (Hs00172878_m1), *HES4* (Hs00368353_g1), *COL1A1*
183 (Hs00164004_m1), *RPL30* (Hs00265497_m1), *RPLP0* (Hs00420895_gH). QuantStudio 6 Flex Real-Time
184 PCR System (Thermo Fisher Scientific) was used to perform RT-qPCR. $\Delta\Delta CT$ was calculated by
185 normalizing treated groups to corresponding controls, and $2^{(-\Delta\Delta CT)}$ was the relative fold change.

186 **CRISPR gene editing in mesenchymal cells**

187 CRISPR gene editing was conducted using the Alt-R™ CRISPR-Cas9 System (IDT). RNP complexes were
188 prepared by combining 2 µl of Alt-R™ S.p. HiFi Cas9 Nuclease V3 (IDT, 1081060) with 3 µl of 200 µM
189 customized sgRNAs, and subsequently mixed with 1×10^5 D4A1 mesenchymal cells suspended in 20 µl of
190 P3 Primary Cell 4D-Nucleofector™ X Kit solution (Lonza, V4XP-3032). The nucleofection procedure was
191 performed utilizing the CM-138 program with the 4D-nucleofector Core Unit (Lonza, AAF-1003B). The
192 NOTCH3 target sequences were: sgRNA1 (GCCACTATGTGAGAACCCCG) and sgRNA2
193 (AGGGTGACAGGGCACC GCG). The sequence of non-targeting sgRNA (NT_sgRNA) was
194 CGTTAATCGCGTATAATACG.

195 **Flow cytometry**

196 To determine the cell surface NOTCH3 expression, cells were detached using a cell scraper, stained with
197 a live/dead dye and anti-NOTCH3 antibody (clone MHN3-21) for over 30 minutes, and analyzed by flow
198 cytometry. Data analysis was performed using FlowJo (Version 10). Cells were first gated based on
199 forward (FSC-A) and side (SSC-A) scatters to exclude debris. Single cells were then selected based on
200 SSC-A versus SSC-W parameters. Dead cells were excluded based on the positive staining of the
201 live/dead dye. The positive cell-surface staining in gated live cells was determined by comparing them to
202 fluorescence minus one as a negative control.

203 **Cell Invasion assay**

204 The ability of cells to invade the surrounding matrix was assessed based on the IncuCyte® S3 3D
205 Spheroid Invasion Assay (Sartorius). Briefly, 5000 cells derived from MRC002, 003, or 004 were added
206 into one well of an ultra-low attachment plate (S-Bio) and treated with DMSO or 10 µM MRK-003 for 3
207 days to form spheroids at 37°C and 5% CO₂ in an incubator. 50% GFR Matrigel (Corning) containing

208 DMSO or MRK-003 was added on top of the spheroids. For D4A1 alone or D4A1 and mKate2+ H1299
209 (1:1) co-cultures, a total of 2000 cells were added into one well of an ultra-low attachment plate
210 (Nexcelom Bioscience) and treated with DMSO or 10 μ M MRK-003 as describe above to allow spheroid
211 formation. Supernatants were collected for assessing COL1A1 production. For CRISPR-edited D4A1 cell,
212 or the co-culturing mKate2+ H1299 with non-targeting control (NT_sgRNA) or NOTCH3 knockout
213 (NOTCH3_sgRNA1, and NOTCH3_sgRNA2) D4A1 cells at a 1:1 ratio, a total of 1000 cells were plated for 3
214 days to form spheroids. For the treatment of the additional γ -secretase inhibitors DAPT (Tocris
215 Bioscience;(15)) and MRK560 (Tocris Bioscience;(16)), 1000 cells without drug treatment were first
216 added into each well of an ultra-low attachment plate to form spheroids for 3 days. GFR Basement
217 Membrane Matrix (Gibco, ThermoFisher) was added onto spheroids in each well. Plates were
218 subsequently centrifuged at 300 g for 5 min at 4°C and incubated for 30 min at 37°C to promote
219 polymerization. Culture medium containing DMSO or γ -secretase inhibitors at a concentration of 10 μ M
220 was added into each well post polymerization and the plates were incubated and monitored by
221 IncuCyte® S3 placed in an incubator at 37°C with 5% CO₂ for indicated hours. Cells that invaded the
222 surrounding matrix were observed using a phase-contrast inverted microscope (magnification, \times 4) and
223 images were captured. Data were analyzed using IncuCyte® S3 Spheroid Software Module (version
224 2021A).

225 **Type I Collagen assay**

226 The concentration of type 1 collagen in supernatants collected above was measured using the human
227 COL1A1 AlphaLISA Detection Kit (PerkinElmer). Standards or samples were added into white Opaque 96-
228 or 384-well microplates (PerkinElmer) and then biotinylated antibodies and beads were added according
229 to the kit instruction. The results were measured using EnVision.

230 **3D cell viability assay**

231 In the cell invasion assay, the cell viability of spheroids derived from MRC002, MRC003, and MRC004
232 was assessed using the CellTiter-Glo® 3D Cell Viability kit (Promega). In brief, the plate and reagents
233 were equilibrated to RT for 30 minutes. The CellTiter-Glo® 3D reagent was added to each well of a 96-
234 well plate containing the spheroids. The plate was then shaken for 5 minutes to induce lysis of the cells.
235 The plate was incubated at RT for additional 30 minutes before measuring the luminescence signal with
236 Envision multilabel reader (PerkinElmer).

237 **Caspase 3/7 assay**

238 IncuCyte® Caspase-3/7 Dyes at a final concentration of 5 uM were used to assess apoptotic effect on
239 H1299-mKate2 expressing cells or D4A1 mesenchymal cells following the compound treatments using
240 IncuCyte® S3. Cells were imaged using both phase contrast and green fluorescence channels with a
241 magnification of 10x. Data were analyzed using IncuCyte® S3 Cell-by-Cell Analysis Software Module
242 (version 2021).

243 **Single-Cell RNA-seq data processing and major cell type annotation**

244 Single-Cell RNA-seq reads were mapped to the human genome (GRCh38) using CellRanger v1.1.0 and
245 then processed through Seurat v3.0(17). Cells with mitochondria percentage over 10% or extreme
246 unique gene totals (less than 500 or over 5,000 per cell) were removed from the analysis. The data after
247 QC inspection was then normalized using SCTransform v0.3.2 (18), and all libraries were merged after
248 batch effect removal through Harmony v1.0 (19). Following the standard protocol provided by Seurat
249 authors, principal components were computed and used for the UMAP dimensionality reduction. Cell
250 clusters were identified at resolution 0.3 and annotated based on prior knowledge. Of note, one cluster,
251 accounting for 0.9% of the total cells, was identified as the proliferating cell cluster. This cluster showed
252 high expression of the proliferation consensus signature (3) and cell-cycle regulation genes such as
253 *STMN1*. Due to the low percentage of proliferating cells within the total cell population, we did not
254 perform cell cycle correction. Two clusters with low cell count were expressing markers of more than
255 one primary cell type and were removed from downstream analysis.

256 **Identification of subpopulations and marker genes**

257 Mesenchymal, lymphatic and vascular endothelial clusters were annotated based on canonical markers
258 such as *COL1A2*, *PROX1*, and *RAMP2*, respectively, for further dimensionality reduction using the
259 FindClusters function in the Seurat package. The differentially expressed genes of mesenchymal cells
260 compared to all other cells were listed in Supplementary Table 3. Mesenchymal cells were further
261 subclustered with resolution of 0.3 and annotated as four subgroups with *FAP*, *PDPN*, *MCAM*, and
262 *ACTA2* expression levels based on previous reports (6,20,21). Vascular endothelial cells were
263 subclustered with resolution of 0.3. Selected markers for EC subclusters' annotation were curated based
264 on a previous report(22). The marker gene lists for mesenchymal cells and endothelial cells were
265 generated using the FindAllMarkers function in Seurat, and the results are provided in Supplementary
266 Table 3 and Table 4, respectively.

267 **Downstream analysis in mesenchymal and endothelial subpopulations**

268 UMAPs, violin plots and bubble plots visualizing expression of genes and markers were generated using
269 Seurat 4.0.6 and ggplot2 v3.3.5, and the color palettes were loaded from ggsci v2.9. Unless otherwise
270 specified, statistical testing in differential expression analysis was the Wilcoxon rank-sum test, and the
271 *p*-values for multiple comparisons were adjusted using the Benjamini-Hochberg method. Heatmaps
272 were generated using pheatmap R package v1.0.12.

273 Subpopulation abundance comparison between T and ANT: The relative abundance of each
274 subpopulation over total mesenchymal or endothelial cell counts was calculated in T and ANT samples,
275 respectively. The Wilcoxon rank-sum test was applied to determine the significance of relative
276 abundance differences between T and ANT in each subpopulation. The figures were styled using ggprism
277 v1.0.3.

278 **Receptor-Ligand analysis**

279 Cell-cell communications between mesenchymal and endothelial subtypes were inferred based on the
280 analysis of differential expressions of known ligand-receptor pairs between T and ANT samples, which
281 was accomplished by following the official workflow of CellChat v1.1.3 (23). The gene expression of
282 endothelial cells and mesenchymal cells after sctransform processing were grouped by T and ANT and
283 loaded into CellChat separately. These two objects went through preprocessing with the following
284 functions using standard parameters: “identifyOverExpressedGenes”,
285 “identifyOverExpressedInteractions” and “projectData”. Then the communication probabilities of T and
286 ANT were analyzed separately using the core functions “computeCommunProb”,
287 “computeCommunProbPathway” and “aggregateNet” with the standard parameters and merged into
288 one object for T vs ANT comparison. Figures were generated using CellChat functions:
289 “netVisual_diffInteraction” for overall pathway enrichment in T vs ANT, “netVisual_aggregate” for circle
290 plots, “netAnalysis_signalingRole_heatmap” for determining signal senders and receivers of top
291 pathways in mesenchymal-endothelial interactions, and “netVisual_chord_gene” for chord plot of
292 NOTCH pathway information flow from endothelial cells to mesenchymal cells.

293 **Leave-one-donor-out validation**

294 To eliminate the potential bias from one donor, we applied a leave-one-out strategy to the differential
295 expression analysis between T and ANT in endothelial and mesenchymal subtypes. One sample was
296 removed in each iteration, and Wilcoxon rank-sum tests were performed between T and ANT to
297 determine the significance of expression enrichment in T. The median and IQR of the *p*-values from the

298 bootstrap analysis were collected for visualization. For expression of each gene by a specific cell type, if
299 the Benjamini-Hochberg p -value was over 0.05 in the all-donor-included iteration, the data would be
300 filtered out.

301 **Bulk RNA-seq based analysis**

302 Expression correlation analysis was performed in LUAD tumor samples only, and Spearman correlation
303 between the average expression of signature genes and scRNA-seq derived fibroblast subset fingerprints
304 was calculated. Differential expression analysis with Benjamini-Hochberg adjusted p -value was
305 performed in TCGA LUAD samples between T and ANT, and the ROC-AUC was calculated by the
306 performance of classifying T using the expression of each tested gene. The Gene set pathway
307 enrichment analysis was performed using the combination of KEGG(24) and GeneGo MetaCore
308 Pathways. The above statistical analysis, and survival analysis, including the Cox proportional hazard
309 model and Kaplan Meier (KM) Survival Analysis, were performed in MATLAB 2021a.

310 **Collection of fingerprints and signatures**

311 The consensus signatures, including stroma-EMT-TGFbeta, Angiogenesis and the 18-gene T-cell inflamed
312 GEP, were published(3). The smooth muscle signature was obtained from the Human Protein Atlas
313 (HPA), including 34 genes in the core smooth muscle cell transcriptome that were predicted as enriched
314 in smooth muscle cells in 50-75% profiled tissues(25). DLL4 and JAG1 stimulation marker signatures
315 were obtained from a publication(26). Fingerprint genes of iCAF, myCAF and apCAF in Elyada et al. were
316 obtained from the publication(5). Fingerprint genes of apCAF in Kerdidani et al. were antigen presenting
317 MHCII+ fibroblast enriched genes collected from the differential expression analysis in the study(27).
318 The gene lists are provided in Supplementary Table 5.

319 **Statistical analysis**

320 Statistical analysis for scRNA-sequencing and bulk RNA-sequencing was performed using the Wilcoxon
321 rank-sum test. Statistical tests for functional assays were conducted using Student t -test. Additional
322 statistical tests are indicated in the legends or corresponding method sections for specific details.
323 Differences were considered statistically significant when $p \leq 0.05$.

324 **Data Availability**

325 The single-cell RNA-seq data generated and analyzed in this study are publicly available in the NCBI
326 BioProject database with the accession number [PRJNA1055415](#), in Gene Expression Omnibus (GEO) at
327 [GSE253013](#), and within the article and its supplementary data files. Bulk RNA-seq databases from the
328 collaboration between Merck & Co., Inc., Rahway, NJ, USA and H. Lee Moffitt Cancer Center (the
329 "Collaboration") and The Cancer Genome Atlas (TCGA) were used in this study. The Collaboration
330 dataset contains 20,000 tumor samples and represents over 25 different cancers, including 1,434 LUAD
331 samples(3). Patient samples were obtained by the H. Lee Moffitt Cancer Center, and the gene
332 expression data was generated using HuRSTA-2a520709 GeneChips (Affymetrix). Additional details
333 regarding the Collaboration dataset and the assay platform (GPL10379) have been published(3) and can
334 be accessed in GEO at [GPL10379](#). TCGA data were obtained from the [Genomic Data Commons Data](#)
335 [Portal](#), and information is available on the [TCGA website](#). Raw data was processed as previously
336 described(3). All other raw data are available upon request from the corresponding author.

337

338 Results

339 scRNA-seq data analysis identifies mesenchymal and other major cell types in LUAD

340 We performed scRNA-seq on a cohort of 9 treatment-naïve patients, out of which 6 had paired
341 adjacent non-tumor (ANT) tissues (Figure 1A). To obtain a representative number of non-immune and
342 immune cells, we sorted live CD45⁻ (non-immune) and CD45⁺ immune cells from 6 out of 9 freshly
343 resected LUAD tumors prior to scRNA-seq. Aiming to match the current standard of fibroblast/stromal-
344 centric scRNA-seq studies, we obtained 256,379 total cells and 13,857 mesenchymal cells, respectively,
345 after quality control and doublet removal. The cells were visualized as a dimensional reduction plot
346 using Uniform Manifold Approximation and Projection (UMAP) (Figure 1B). Eight distinct cell types were
347 identified by using RNA expression of canonical markers (Figure 1B-C). In-depth investigation of non-
348 stromal cell types identified diverse cell subclusters in the TME that are similar to previous scRNA-seq
349 studies in non-small cell lung cancer (NSCLC) (Supplementary Figure 1A-D)(8,10,28). We next sought to
350 decipher mesenchymal cell heterogeneity and its intercellular network to interrogate dysregulated
351 pathways in the tumor stroma.

352 Four distinct mesenchymal subpopulations in lung tumor stroma

353 To characterize the heterogeneity of mesenchymal cells in LUAD, we first subclustered them and
354 observed four distinct clusters: *FAP*⁺*PDPN*⁺ CAFs(5,6,20,29), *MCAM*⁺*ACTA2*⁺ pericytes(21), *ACTA2*⁺ SMCs,
355 and lung resident fibroblasts (LRFs) (Figure 2A-B). LRFs were predominantly derived from ANT tissues
356 (Figure 2C; *p*-value < 0.001), and SMCs comprised of cells from both tumors and ANTs. Remarkably,
357 *MCAM*⁺*ACTA2*⁺ pericytes and *FAP*⁺*PDPN*⁺ CAFs were almost exclusively originated from tumors (*p*-value
358 = 0.002, for both subtypes). We confirmed the presence of *FAP*⁺*PDPN*⁺ CAFs and *MCAM*⁺ pericytes by
359 flow cytometry (Figure 2D). Our annotation of the four clusters was further confirmed by investigating
360 additional marker gene sets expressed by these cells (Figure 2E, Supplementary Figure 2A-C and Table
361 3). For instance, pericytes expressed the well-established marker gene *PDGFRB*. SMCs were positive for
362 previously described genes that have functional impacts on vascular SMCs, such as *MFAP4*. In contrast
363 to other clusters, *FAP*⁺*PDPN*⁺ CAFs showed a gene expression spectrum characterized by a high
364 expression of collagens and matrix-degrading enzymes, indicating these cells may have a myofibroblast
365 phenotype of promoting ECM deposition and remodeling (Supplementary Table 3).

366 We next explored the phenotypes of mesenchymal cell clusters by correlating the marker gene
367 sets of the four clusters with the consensus bulk RNA-seq signatures derived from much larger lung
368 adenocarcinoma cohorts, including the Collaboration dataset, TCGA, and the Human protein Atlas(3,25).
369 The stroma/EMT/TGF β and angiogenesis signatures represent canonical biological processes that are
370 common across different tumor types and are associated with resistance to ICB monotherapy(3). The
371 marker gene sets of both CAFs and pericytes were strongly correlated with the Stroma/EMT/TGF β
372 signature compared to the other two clusters, whereas pericyte marker genes were closely related to
373 the angiogenesis signature (Figure 2F). Consistent with our annotation, the marker gene set of SMCs
374 showed the highest correlation with the muscle signature. These observations were further confirmed in
375 the TCGA LUAD patient cohort (Supplementary Figure 2D). Given that the stroma/EMT/TGF β signature is
376 associated with a “myCAF” phenotype(6,7), we further explored the previously defined “myCAF” and
377 “iCAF” phenotypes by mapping the related gene signatures to the four clusters. The myCAF marker
378 genes were most enriched in CAFs and then in pericytes, whereas iCAF marker genes were enriched in
379 LRFs (Figure 2G). Similarly, a gene signature of antigen-presenting CAFs (apCAFs), derived from a prior
380 NSCLC study (27), was also enriched in LRFs and showed the highest expression in myeloid cells
381 (Supplementary Figure 2E-F). Given that CAFs are characterized by their diverse phenotypes and
382 heterogeneity, we compared the expression levels of “myCAF” and “iCAF” signatures within the CAF
383 subclusters (Supplementary Figure 2G). CAF-S3 exhibited the highest expression of the “myCAF”
384 signature (Supplementary Figure 2H). On the other hand, although CAF-S7 showed the highest
385 expression of the “iCAF” signature among all CAF subclusters, its expression was lower compared to the
386 levels observed in LRFs (Supplementary Figure 2H-I). These findings indicate the existence of
387 heterogeneity within the CAF subclusters and suggest that the CAF cluster as a whole adopts a myCAF-
388 like phenotype in this cohort of LUAD. Notably, this cell cluster also has the highest correlation with
389 stromal/EMT/TGF β bulk RNA-seq signature, which has demonstrated clinical association with ICB
390 resistance(3).

391 **Neighborhood analysis of tumor-associated mesenchymal populations**

392 Next, we sought to understand how the spatial organization of cell types dictates intercellular
393 interactions that create and maintain a reactive tumor stroma. To dissect cell neighbors interacting with
394 the three major mesenchymal subpopulations: *FAP*⁺*PDPN*⁺ CAFs, *MCAM*⁺*ACTA2*⁺ pericytes, *ACTA2*⁺
395 SMCs, we exploited a high-dimensional imaging technique known as IMC and multiplexed 18 markers in
396 an independent cohort of 7 histologically confirmed LUAD samples (Figure 3A-B). We found that

397 MCAM⁺ and ACTA2⁺ cells comprised a thin layer surrounding CD31⁺ blood vessels and were indicative
398 of MCAM⁺ACTA2⁺ pericytes or ACTA2⁺ vascular SMCs identified in the scRNA-seq data. In contrast, FAP⁺
399 collagen I⁺ CAFs resided in stromal regions between vascular zones and E-cadherin⁺ tumor parenchyma.
400 Cell segmentation masks and t-SNE plots for each marker were generated from 7 samples for further
401 analysis and visualization (Figure 3C and Supplementary Figure 3A).

402 To enable quantitative spatial interrogation of cell-to-cell interactions, we used PhenoGraph
403 (30) and identified 25 clusters characterized by specific epitopes across 7 donors (Figure 3D). The
404 annotation of each cluster can be found in Supplementary Table 6. Cluster 8, and 12 were FAP⁺ CAFs
405 with uneven expression of collagen I and CD90. We identified a CD31⁺MCAM⁺ population (cluster 7) that
406 likely contained both CD31⁺ ECs and surrounding MCAM⁺ pericytes. The mixture of the lineage markers
407 was likely due to the low resolution of IMC to separate ECs and surrounding MCAM⁺ pericytes. This
408 result indicates the geographic proximity of CD31⁺ and MCAM⁺ cells. Cluster 16 was a mixture of SMCs
409 and pericytes with ACTA2 and MCAM expression, whereas cluster 18 expressed MCAM as well as
410 additional mesenchymal cell markers CD90 and Vimentin. We then performed neighborhood analysis to
411 investigate significant interactions or avoidances of cell-cell neighbors in tumors (Figure 3E and
412 Supplementary Figure 3B). In over 50% of tested images, the FAP⁺ CAF cluster 8 significantly interacted
413 with CAFs (cluster 8 and 12), CD4⁺ T cells (cluster 2), CD8⁺ T cells (cluster 10), pericytes and vSMCs
414 (cluster 16, 18, and 7), and ECs (cluster 6 and 7) (Figure 3E, *p*-value <0.01). Similarly, pericytes and
415 vSMCs (cluster 16 and 7) had robust inter-cellular interactions with FAP⁺ CAFs and T cells in 50% of
416 tested images. Overall, the neighborhood analysis reveals a close topographical association between
417 tumor-associated mesenchymal cells and endothelial/T cells.

418 **Ligand-receptor analysis identifies dysregulated NOTCH3 signaling in tumor stroma**

419 Previous studies have focused on delineating the interactions between mesenchymal and T cells
420 to sculpt an immunosuppressive TME(4,31,32). Although ECs are emerging as a key player in pathogenic
421 stromal remodeling in non-cancerous indications(26,33,34), little is known about how ECs cooperate
422 with mesenchymal cells to remodel and activate tumor stroma in LUAD. Thus, we investigated the
423 endothelial-mesenchymal crosstalk and dissected the underlying molecular determinants. We identified
424 both vascular and lymphatic ECs. The lymphatic ECs formed a unique cluster in the UMAP containing all
425 primary cell types (Figure 4A), and the vascular ECs were re-clustered into 7 subclusters. Subcluster N1,
426 N2, and N3 were significantly enriched in ANT samples, while subcluster T1, T2, and T3 were enriched in
427 tumors (Figure 4B). Similar to previous findings(22), Endo T1 was an activated postcapillary vein EC

428 cluster expressing *ACKR1* and high-endothelial-venule EC marker *IGFBP7*; Endo T2 and T3 were *PLVAP*^{high}
429 immature neovascular ECs; Endo G1 expressed several arterial EC markers, including *DKK2*, *GJA5*, *FBLN5*,
430 and *SERPINE2*, and thus was an arterial EC cluster (Figure 4C, Supplementary Table 5).

431 To understand intercellular communications based on the differential expression of ligand-
432 receptor pairs between mesenchymal and ECs, we performed statistical analysis using CellChat, with a
433 focus on predicted cell-cell contact pathways that were specifically enriched in tumors(23). We
434 prioritized 11 signaling pathways with the highest statistical measurements of information flow in
435 tumors versus ANTs (Figure 4D). The top 3 pathways were ESAM, MHC-II and NOTCH signaling, which
436 were also among the top 5 when considering all potential ligand-receptor interactions in the CellChatDB
437 (Supplementary Figure 4A). Some of the 11 pathways, such as ESAM, SEMA6, and ADGRE5, were
438 predominantly driven by predicted intracellular interactions within ECs or mesenchymal cells (Figure 4E,
439 Supplementary Figure 4B). To understand how the predicted interactions between cell types may
440 modulate the phenotype of mesenchymal cells, we filtered for predictions of ligands from ECs and
441 receptors from mesenchymal cells. The top 2 pathways that met the requirements were MHC-II and
442 NOTCH (Figure 4E and Supplementary Figure 4B-C).

443 Given the established involvement of NOTCH signaling in fibrosis(26,33), we sought to
444 determine its prevalence in the tumor stroma of LUAD. Multiple endothelial subtypes contributed to the
445 ligand expression, whereas *NOTCH3* was the major receptor expressed mainly by pericytes, and by CAFs
446 at a lower level (Figure 4F, Supplementary Figure 4D). To validate that the significant expression of
447 NOTCH pathway ligand-receptor pairs in tumors is not determined by a single donor, we performed a
448 leave-one-donor-out analysis. The distributions of *p*-values of ligand-receptor pairs in each subtype were
449 visualized (Figure 4G-H). Given that the number of pericytes in ANT was too low to perform statistical
450 analysis ($n < 10$, Figure 2C), we compared the enrichment of NOTCH receptor genes in all mesenchymal
451 cells and other three subtypes and found the significant enrichment of *NOTCH3* across donors (Figure
452 4G). Endo G1 had significant enrichment of NOTCH ligands *DLL4*, *JAG1* and *JAG2* across donors, whereas
453 the increased ligand expression in other subtypes had a larger donor-driven variation (Figure 4H). We
454 further confirmed the specific NOTCH3 expression on MCAM⁺ pericytes within the TME by
455 immunofluorescence staining (Figure 4I). Given that there are limited donors in our scRNA-seq dataset,
456 we evaluated the differential NOTCH receptor expression in a larger cohort utilizing the TCGA dataset,
457 which includes 530 LUAD T samples and 59 LUAD ANT samples. *NOTCH3* is the only NOTCH receptor that
458 significantly upregulated in tumors (Figure 4J).

459 To further explore the potential downstream effects of NOTCH dysregulation in LUAD tumor
460 samples, we evaluated the activation of this pathway by cross-referencing the NOTCH activation scores
461 developed by Wei et al., which was generated by *in-vitro* JAG1 and DLL4 stimulation of synovial
462 fibroblasts(26), and the canonical NOTCH-response markers in our scRNA-seq dataset(35,36). NOTCH
463 activation scores and the canonical NOTCH responsive markers were significantly enriched in all
464 mesenchymal cells from tumor samples (Supplementary Figure 4E). Similarly, by investigating
465 mesenchymal subtypes, CAFs and pericytes had significant enrichment of both activation scores
466 compared to LRFs (Supplementary Figure 4F). Our observation indicates that the increased expression of
467 NOTCH ligand-receptor pairs translates into NOTCH signaling activation in mesenchymal cells in tumors.

468 **Blocking NOTCH signaling decreases collagen production and cell invasion**

469 To interrogate the role of NOTCH signaling in regulating the function of tumor-associated
470 mesenchymal cells, we expanded stromal cells from freshly-resected tumor samples and were able to
471 propagate MCAM⁺NOTCH3⁺ cells from 3 independent donors as indicated by flow staining (Figure 5A).
472 We then co-cultured these cells with primary human pulmonary artery ECs that served as the source of
473 NOTCH ligands. Subsequently, the co-culture was treated with MRK003, a well-characterized γ -secretase
474 inhibitor known to block the NOTCH pathway and function as a pan-NOTCH inhibitor (14,37). MRK003
475 treatment robustly reduced the expression of several downstream NOTCH target genes in the
476 mesenchymal and EC co-cultures (Figure 5B). After confirming the inhibition of NOTCH pathway, we
477 further investigated if MRK003 treatment affects the expression of genes associated with ECM
478 remodeling and cell adhesion in the co-culture. We found significant down-regulation of several fibrillar
479 collagen genes, including *COL1A1*, as well as the fibrotic gene *CTGF* (Figure 5C). We also confirmed that
480 MRK003 treatment significantly reduced *COL1A1* at protein levels (Figure 5D). To further investigate the
481 role of NOTCH3 in regulating collagen expression, we utilized two siRNAs to downregulate *NOTCH3*
482 mRNA levels by 70% in the EC and mesenchymal cell co-cultures. Consequently, we observed reduced
483 cell surface NOTCH3 expression, accompanied by a significant reduction in *COL1A1* expression
484 (Supplementary Figure 5A-E).

485 Given that enhanced collagen deposition promotes cell invasion in the TME(38,39), we further
486 explored how NOTCH inhibition affects the invasiveness of mesenchymal cells. Cells were embedded in
487 three-dimensional matrix in the presence of DMSO or MRK003, and the cell invading area was
488 quantified. MRK003 treated cells showed a reduction in the invading area compared to control cells in
489 all donors tested, with significant inhibition seen in two of the three donors (Figure 5E-F). We further

490 tested a high NOTCH3-expressing mesenchymal cell line derived from an independent donor (D4A1) to
491 confirm the inhibitory effect of MRK003 on cell invasion (Figure 5G-H). We tested two additional γ -
492 secretase inhibitors, DAPT(15), and MRK560 (16), that block NOTCH pathway signaling. MRK560
493 significantly reduced mesenchymal cell invasion, whereas DAPT treatment showed a trend of
494 suppressing cell invasion that did not reach statistical significance (Supplementary Figure 6A). Since
495 previous reports show that tumor-associated mesenchymal cells in promote tumor cell invasion and
496 metastasis(40,41), we investigated the potential of inhibiting the NOTCH pathway to suppress their pro-
497 invasive effect. We co-cultured a fluorescence-labeled metastatic NSCLC line H1299 with or without the
498 D4A1 mesenchymal cells in the matrix and tracked the tumor cell invasion area reflected by
499 fluorescence intensity. The presence of D4A1 mesenchymal cells increased the invasive capacity of
500 H1299, and MRK003 treatment robustly suppressed the invasion of H1299 co-cultured with D4A1 cells
501 to the same level as H1299 alone (Figure 5I). We also observed that MRK003 treatment directly
502 suppressed H1299 invasion (Figure 5I).

503 To determine whether the impaired invasion is associated with changes in cell growth or ECM
504 production, we quantified viable cells or monitored cell death in mesenchymal cells over time. We did
505 not observe any significant changes in the number of viable cells or the occurrence of a cell apoptosis
506 phenotype, as indicated by caspase 3 and 7 signals (Supplementary Figure 6B-D). However, MRK003
507 treatment did significantly change COL1A1 production in mesenchymal cells (Supplementary Figure 6E).
508 In contrast, MRK003 treatment in H1299 cells significantly increased caspase 3 and 7 signals, indicating
509 the induction of cytotoxic effects (Supplementary Figure 6F). The cytotoxic effects led to a decrease in
510 cell numbers, as evident by the reduced red signal intensity of the H1299 spheroids (Supplementary
511 Figure 6G). This data suggests that MRK003 suppresses the invasive capacity of H1299 by inducing cell
512 death. To further understand whether mesenchymal cells can promote tumor cell invasion in a NOTCH3-
513 dependent manner, we utilized CRISPR gene editing to generate NOTCH3 knockout D4A1 mesenchymal
514 cells and found NOTCH3 knockout cells exhibited reduced invasive capacity (Supplementary Figure 6H-I).
515 Subsequently, we co-cultured H1299 cells with mesenchymal cells that were either NOTCH3 wild-type or
516 knockout and observed reduced invasion in H1299 cells co-cultured with NOTCH3 knockout
517 mesenchymal cells (Supplementary Figure 6J). The data suggest that mesenchymal cells can promote
518 tumor invasion through a NOTCH3-mediated effect.

519 To gain better insight into the function of NOTCH3 in tumor cells, we assessed its expression in
520 H1299 cells. We found limited cell surface expression of NOTCH3 in H1299 cells (Supplementary Figure

521 6K). Additionally, by analyzing our scRNA-seq dataset, we observed minimal NOTCH3 expression in
522 epithelial cells (Supplementary Figure 6L-M). Based on the limited expression of NOTCH3 in tumor cells,
523 we did not further investigate its role in regulating cell invasion of H1299 cells. The observed effect of
524 MRK003 treatment could potentially be attributed to the presence of NOTCH1 expression in H1299 cells
525 (42). Consequently, MRK003 may also inhibit NOTCH1 signaling in H1299 cells, leading to reduced cell
526 death and invasion. In summary, our in-vitro data demonstrates the functional role of NOTCH signaling
527 in promoting mesenchymal cell invasion, potentially through the regulation of ECM molecule
528 production, such as COL1A1.

529 **Clinical relevance of NOTCH3 in modulating tumor stroma and predicting patient survival**

530 Our *in-vitro* functional data suggests that the activation of NOTCH pathway can regulate
531 collagen production and ECM remodeling. To explore the clinical relevance of this observation, we
532 evaluated the association of *NOTCH3* expression with global gene expression in two independent LUAD
533 patient cohorts (Figure 6A and Supplementary Table 7). *COL1A1* was among the top genes with the
534 highest correlation with *NOTCH3*. We further selected the genes with Spearman correlation coefficients
535 over 0.4 and subjected them to pathway enrichment analysis (Figure 6B). These genes were enriched in
536 pathways related to cell adhesion, ECM remodeling, TGF β -induced fibroblast migration and ECM
537 production.

538 To examine the impact of NOTCH signaling on patient prognosis, we analyzed the association
539 between the expression of each NOTCH pathway gene and overall patient survival in 1,434 LUAD
540 samples in the Collaboration dataset. While NOTCH ligands *JAG1*, *JAG2*, and *DLL3* were associated with
541 worse patient survival outcome, *NOTCH3* expression had no correlation (Figure 6C). Given that *NOTCH3*
542 is a mesenchymal cell-specific gene, we hypothesized that its predictive value for survival may be limited
543 to stromal-rich patients. After dichotomizing patient samples into stroma-low and stroma-high
544 subgroups at the median expression level of the consensus stroma/EMT/TGF β signature, we observed a
545 lack of *NOTCH3* association in the stroma-low group (Figure 6D). However, in the stroma-high group,
546 *NOTCH3* and its ligand, *JAG1*, emerged as worse prognostic markers (Figure 6E). Given the pivotal role of
547 mesenchymal cells in driving ICB resistance(3,4,7,43), we further examined the impact of *NOTCH3*
548 expression on the prognostic value of an 18-gene T-cell-inflamed gene expression profile (GEP) that
549 predicts better response to a PD-1 antagonist pembrolizumab across multiple tumor types(43). Again,
550 we binned LUAD samples at the median *NOTCH3* expression and found that GEP served as a good
551 prognosis marker only in the *NOTCH3*-low subgroup (Figure 6F-G). This suggests that high *NOTCH3*

552 expression potentially impedes the anti-tumor effects mediated by T cells, which are crucial for effective
553 responses to ICB like PD-1 antagonists. To further explore the clinical relevance of *NOTCH3* expression
554 and its potential association with ICB resistance, we examined the correlation between *NOTCH3*
555 expression and two consensus gene signatures linked to resistance to anti-PD1 monotherapy in solid
556 pan-tumor types: stroma/EMT/TGF β and angiogenesis (3). Our analysis revealed a robust positive
557 correlation between *NOTCH3* expression and both gene signatures (Figure 6H and Supplementary Table
558 7).

559 Additionally, we examined the relationship between oncogenic mutations and *NOTCH3*
560 expression using both the TCGA and the Collaboration datasets. Our finding revealed a significant
561 increase in *NOTCH3* expression among patients with K-RAS or KEAP1 mutation compared to wild-type in
562 both datasets (Supplementary Figure 7A-B). Together, these results underscore the potential clinical
563 relevance of *NOTCH3* as a stromal-specific target. Further investigations utilizing pre-clinical models are
564 warranted to fully comprehend the crucial role of *NOTCH3* in tumor stroma remodeling and to evaluate
565 the therapeutic potential of combining *NOTCH3* antagonism with ICB monotherapy.

566 Discussion

567 In this study, we have resolved the cellular composition of epithelial, immune, and stromal
568 compartments in freshly resected tumor tissue from a cohort of nine treatment-naïve lung
569 adenocarcinoma patients with a focus on deconvoluting stromal heterogeneity. Using this approach, we
570 have identified the enrichment of *FAP*⁺*PDPN*⁺ CAFs and tumor associated *MCAM*⁺*ACTA2*⁺ pericytes in
571 tumors compared to adjacent non-tumor tissues. We further map out the spatial architecture of these
572 three major compartments by imaging mass cytometry and demonstrate a close spatial relationship
573 between CAFs, pericytes, and ECs. Ligand-receptor interaction analysis among stromal lineages reveals
574 the increased expression of *NOTCH3* in both CAFs and pericytes, whereas several NOTCH ligands are
575 elevated in tumor-associated EC subsets, highlighting a dysregulated *NOTCH3* pathway in the tumor
576 stroma (Figure 6I). The multimodal characterization of the TME in LUAD underscores the importance of
577 the “myCAF”-like *FAP*⁺*PDPN*⁺ CAFs, and necessitates a more comprehensive investigation into the critical
578 involvement of *NOTCH3* in tumor stroma remodeling, such as genetically engineered mouse models.

579 *NOTCH* signaling is a conserved pathway that plays a critical role in developmental cell-fate
580 decisions and has been linked to multiple diseases including cancer(44,45); however, *NOTCH*-targeted
581 therapy is not clinically successful(46). One potential reason lies in the inadequate characterization of

582 the expression and functions of each NOTCH receptor in pathological contexts, as different NOTCH
583 receptors have contradictory biological effects(46). For example, activation of NOTCH1/2 in CD8-T cells
584 triggers a robust and sustained anti-tumor response, resulting in increased IFN γ production and reduced
585 tumor burden(47). Thus, nonselective inhibition of the NOTCH pathway will potentially curb anti-tumor
586 immune responses. Recent scRNA-seq studies underscore the importance of NOTCH3, among other
587 NOTCH receptors, during pathological tissue remodeling in human liver cirrhosis and rheumatoid
588 arthritis(26,33). Tuning down NOTCH signaling in human hepatic stellate cells decreases fibrillar collagen
589 production(33), whereas blocking NOTCH3 signaling either by genetic or pharmacological inhibition
590 attenuates disease severity in an inflammatory arthritis model(26).

591 In this study, we build on the body of knowledge that has implicated the function of NOTCH3
592 during pathogenic stromal remodeling and further demonstrate the dysregulated NOTCH3 signaling in the
593 perivascular niche of the tumor stroma in lung adenocarcinoma. Our data indicates the reciprocal
594 interaction of NOTCH3 expressed by pericytes and CAFs and its ligands, such as JAG1 and DLL4, on tumor-
595 associated ECs is likely to shape the tumor-permissive TGF β -driven “myCAF” phenotype. We further
596 utilized *in-vitro* functional assays to demonstrate that suppressing NOTCH signaling reduces collagen
597 production and matrix invasion of mesenchymal cells. Mesenchymal cells can promote tumor cell invasion
598 in a NOTCH3-dependent manner. Our finding regarding the potential connection between NOTCH3 and
599 COL1A1 expression has also been observed in several *in vivo* fibrosis models(48,49). Further investigation
600 is needed to understand the mechanistic role of NOTCH3 in regulating the expression of COL1A1 or other
601 ECM components and whether increased mesenchymal cell invasiveness is directly or indirectly impacted
602 by COL1A1 within the context of lung cancer *in vivo*.

603 By investigating patient-derived transcriptomic data, we find that *NOTCH3* expression is
604 associated with poor survival in patients with the high expression of the TGF β -EMT signature. While the
605 T-cell-inflamed GEP biomarker does not exhibit prognostic significance in patients with high *NOTCH3*
606 expression, it becomes notably significant in patients with low *NOTCH3* expression. Given that the T-cell-
607 inflamed GEP is a predictive biomarker for response to immunotherapy(43), investigating the potential of
608 NOTCH3 antagonism as a combination strategy to modulate tumor stroma in conjunction with ICB
609 presents an important avenue that warrants further exploration.

610 **Acknowledgments**

611 We would like to thank Dr. Milena Rosa Hornburg for providing gene signatures and input on the
612 manuscript. We also acknowledge Amber Montano and Dr. Alejandro for sharing protocols. This work
613 was supported by the Merck & Co., Inc., Rahway, NJ, USA Research Laboratories Postdoctoral Research
614 Program.

615

616 **References**

- 617 1. Myers DJ, Wallen JM. Lung Adenocarcinoma. StatPearls. Treasure Island (FL)2023.
- 618 2. Onoi K, Chihara Y, Uchino J, Shimamoto T, Morimoto Y, Iwasaku M, *et al.* Immune Checkpoint
619 Inhibitors for Lung Cancer Treatment: A Review. *J Clin Med* **2020**;9
- 620 3. Cristescu R, Nebozhyn M, Zhang C, Albright A, Kobie J, Huang L, *et al.* Transcriptomic
621 Determinants of Response to Pembrolizumab Monotherapy across Solid Tumor Types. *Clin*
622 *Cancer Res* **2022**;28:1680-9
- 623 4. Mariathasan S, Turley SJ, Nickles D, Castiglioni A, Yuen K, Wang Y, *et al.* TGFbeta attenuates
624 tumour response to PD-L1 blockade by contributing to exclusion of T cells. *Nature*
625 **2018**;554:544-8
- 626 5. Elyada E, Bolisetty M, Laise P, Flynn WF, Courtois ET, Burkhart RA, *et al.* Cross-Species Single-Cell
627 Analysis of Pancreatic Ductal Adenocarcinoma Reveals Antigen-Presenting Cancer-Associated
628 Fibroblasts. *Cancer Discov* **2019**;9:1102-23
- 629 6. Dominguez CX, Muller S, Keerthivasan S, Koeppen H, Hung J, Gierke S, *et al.* Single-Cell RNA
630 Sequencing Reveals Stromal Evolution into LRRC15(+) Myofibroblasts as a Determinant of
631 Patient Response to Cancer Immunotherapy. *Cancer Discov* **2020**;10:232-53
- 632 7. Krishnamurty AT, Shyer JA, Thai M, Gandham V, Buechler MB, Yang YA, *et al.* LRRC15(+)
633 myofibroblasts dictate the stromal setpoint to suppress tumour immunity. *Nature*
634 **2022**;611:148-54
- 635 8. Lambrechts D, Wauters E, Boeckx B, Aibar S, Nittner D, Burton O, *et al.* Phenotype molding of
636 stromal cells in the lung tumor microenvironment. *Nat Med* **2018**;24:1277-89
- 637 9. Gentles AJ, Hui AB, Feng W, Azizi A, Nair RV, Bouchard G, *et al.* A human lung tumor
638 microenvironment interactome identifies clinically relevant cell-type cross-talk. *Genome Biol*
639 **2020**;21:107
- 640 10. Kim N, Kim HK, Lee K, Hong Y, Cho JH, Choi JW, *et al.* Single-cell RNA sequencing demonstrates
641 the molecular and cellular reprogramming of metastatic lung adenocarcinoma. *Nat Commun*
642 **2020**;11:2285
- 643 11. Wagle N, Berger MF, Davis MJ, Blumenstiel B, Defelice M, Pochanard P, *et al.* High-throughput
644 detection of actionable genomic alterations in clinical tumor samples by targeted, massively
645 parallel sequencing. *Cancer Discov* **2012**;2:82-93
- 646 12. Xiang H, Ramil CP, Hai J, Zhang C, Wang H, Watkins AA, *et al.* Cancer-Associated Fibroblasts
647 Promote Immunosuppression by Inducing ROS-Generating Monocytic MDSCs in Lung Squamous
648 Cell Carcinoma. *Cancer Immunol Res* **2020**;8:436-50
- 649 13. Schapiro D, Jackson HW, Raghuraman S, Fischer JR, Zanotelli VRT, Schulz D, *et al.* histoCAT:
650 analysis of cell phenotypes and interactions in multiplex image cytometry data. *Nat Methods*
651 **2017**;14:873-6
- 652 14. Mizuma M, Rasheed ZA, Yabuuchi S, Omura N, Campbell NR, de Wilde RF, *et al.* The gamma
653 secretase inhibitor MRK-003 attenuates pancreatic cancer growth in preclinical models. *Mol*
654 *Cancer Ther* **2012**;11:1999-2009
- 655 15. Feng J, Wang J, Liu Q, Li J, Zhang Q, Zhuang Z, *et al.* DAPT, a gamma-Secretase Inhibitor,
656 Suppresses Tumorigenesis, and Progression of Growth Hormone-Producing Adenomas by
657 Targeting Notch Signaling. *Front Oncol* **2019**;9:809
- 658 16. Best JD, Smith DW, Reilly MA, O'Donnell R, Lewis HD, Ellis S, *et al.* The novel gamma secretase
659 inhibitor N-[cis-4-[(4-chlorophenyl)sulfonyl]-4-(2,5-difluorophenyl)cyclohexyl]-1,1,1-
660 trifluoromethanesulfonamide (MRK-560) reduces amyloid plaque deposition without evidence
661 of notch-related pathology in the Tg2576 mouse. *J Pharmacol Exp Ther* **2007**;320:552-8

- 662 17. Stuart T, Butler A, Hoffman P, Hafemeister C, Papalexi E, Mauck WM, 3rd, *et al.* Comprehensive
663 Integration of Single-Cell Data. *Cell* **2019**;177:1888-902 e21
- 664 18. Hafemeister C, Satija R. Normalization and variance stabilization of single-cell RNA-seq data
665 using regularized negative binomial regression. *Genome Biol* **2019**;20:296
- 666 19. Korsunsky I, Millard N, Fan J, Slowikowski K, Zhang F, Wei K, *et al.* Fast, sensitive and accurate
667 integration of single-cell data with Harmony. *Nat Methods* **2019**;16:1289-96
- 668 20. Cremasco V, Astarita JL, Grauel AL, Keerthivasan S, MacIsaac K, Woodruff MC, *et al.* FAP
669 Delineates Heterogeneous and Functionally Divergent Stromal Cells in Immune-Excluded Breast
670 Tumors. *Cancer Immunol Res* **2018**;6:1472-85
- 671 21. Yamazaki T, Mukoyama YS. Tissue Specific Origin, Development, and Pathological Perspectives
672 of Pericytes. *Front Cardiovasc Med* **2018**;5:78
- 673 22. Goveia J, Rohlenova K, Taverna F, Treps L, Conradi LC, Pircher A, *et al.* An Integrated Gene
674 Expression Landscape Profiling Approach to Identify Lung Tumor Endothelial Cell Heterogeneity
675 and Angiogenic Candidates. *Cancer Cell* **2020**;37:421
- 676 23. Jin S, Guerrero-Juarez CF, Zhang L, Chang I, Ramos R, Kuan CH, *et al.* Inference and analysis of
677 cell-cell communication using CellChat. *Nat Commun* **2021**;12:1088
- 678 24. Kanehisa M, Goto S. KEGG: kyoto encyclopedia of genes and genomes. *Nucleic Acids Res*
679 **2000**;28:27-30
- 680 25. Norreen-Thorsen M, Struck EC, Oling S, Zwahlen M, Von Feilitzen K, Odeberg J, *et al.* A human
681 adipose tissue cell-type transcriptome atlas. *Cell Rep* **2022**;40:111046
- 682 26. Wei K, Korsunsky I, Marshall JL, Gao A, Watts GFM, Major T, *et al.* Notch signalling drives
683 synovial fibroblast identity and arthritis pathology. *Nature* **2020**;582:259-64
- 684 27. Kerdidani D, Aerakis E, Verrou KM, Angelidis I, Douka K, Maniou MA, *et al.* Lung tumor MHCII
685 immunity depends on in situ antigen presentation by fibroblasts. *J Exp Med* **2022**;219
- 686 28. Cheng S, Li Z, Gao R, Xing B, Gao Y, Yang Y, *et al.* A pan-cancer single-cell transcriptional atlas of
687 tumor infiltrating myeloid cells. *Cell* **2021**;184:792-809 e23
- 688 29. Ohlund D, Elyada E, Tuveson D. Fibroblast heterogeneity in the cancer wound. *J Exp Med*
689 **2014**;211:1503-23
- 690 30. Levine JH, Simonds EF, Bendall SC, Davis KL, Amir el AD, Tadmor MD, *et al.* Data-Driven
691 Phenotypic Dissection of AML Reveals Progenitor-like Cells that Correlate with Prognosis. *Cell*
692 **2015**;162:184-97
- 693 31. Hornburg M, Desbois M, Lu S, Guan Y, Lo AA, Kaufman S, *et al.* Single-cell dissection of cellular
694 components and interactions shaping the tumor immune phenotypes in ovarian cancer. *Cancer*
695 *Cell* **2021**;39:928-44 e6
- 696 32. Grout JA, Sirven P, Leader AM, Maskey S, Hector E, Puisieux I, *et al.* Spatial Positioning and
697 Matrix Programs of Cancer-Associated Fibroblasts Promote T-cell Exclusion in Human Lung
698 Tumors. *Cancer Discov* **2022**;12:2606-25
- 699 33. Ramachandran P, Dobie R, Wilson-Kanamori JR, Dora EF, Henderson BEP, Luu NT, *et al.*
700 Resolving the fibrotic niche of human liver cirrhosis at single-cell level. *Nature* **2019**;575:512-8
- 701 34. Zeisberg EM, Tarnavski O, Zeisberg M, Dorfman AL, McMullen JR, Gustafsson E, *et al.*
702 Endothelial-to-mesenchymal transition contributes to cardiac fibrosis. *Nat Med* **2007**;13:952-61
- 703 35. Borggreffe T, Oswald F. The Notch signaling pathway: transcriptional regulation at Notch target
704 genes. *Cell Mol Life Sci* **2009**;66:1631-46
- 705 36. Proweller A, Pear WS, Parmacek MS. Notch signaling represses myocardin-induced smooth
706 muscle cell differentiation. *J Biol Chem* **2005**;280:8994-9004
- 707 37. Stoeck A, Lejnine S, Truong A, Pan L, Wang H, Zang C, *et al.* Discovery of biomarkers predictive of
708 GSI response in triple-negative breast cancer and adenoid cystic carcinoma. *Cancer Discov*
709 **2014**;4:1154-67

- 710 38. Budden T, Gaudy-Marqueste C, Porter A, Kay E, Gurung S, Earnshaw CH, *et al.* Ultraviolet light-
711 induced collagen degradation inhibits melanoma invasion. *Nat Commun* **2021**;12:2742
- 712 39. Li M, Wang J, Wang C, Xia L, Xu J, Xie X, *et al.* Microenvironment remodeled by tumor and
713 stromal cells elevates fibroblast-derived COL1A1 and facilitates ovarian cancer metastasis. *Exp*
714 *Cell Res* **2020**;394:112153
- 715 40. Pelon F, Bourachot B, Kieffer Y, Magagna I, Mermet-Meillon F, Bonnet I, *et al.* Cancer-associated
716 fibroblast heterogeneity in axillary lymph nodes drives metastases in breast cancer through
717 complementary mechanisms. *Nat Commun* **2020**;11:404
- 718 41. Attieh Y, Clark AG, Grass C, Richon S, Pocard M, Mariani P, *et al.* Cancer-associated fibroblasts
719 lead tumor invasion through integrin-beta3-dependent fibronectin assembly. *J Cell Biol*
720 **2017**;216:3509-20
- 721 42. Huang J, Chen Y, Li J, Zhang K, Chen J, Chen D, *et al.* Notch-1 Confers Chemoresistance in Lung
722 Adenocarcinoma to Taxanes through AP-1/microRNA-451 Mediated Regulation of MDR-1. *Mol*
723 *Ther Nucleic Acids* **2016**;5:e375
- 724 43. Cristescu R, Mogg R, Ayers M, Albright A, Murphy E, Yearley J, *et al.* Pan-tumor genomic
725 biomarkers for PD-1 checkpoint blockade-based immunotherapy. *Science* **2018**;362
- 726 44. Dontu G, Jackson KW, McNicholas E, Kawamura MJ, Abdallah WM, Wicha MS. Role of Notch
727 signaling in cell-fate determination of human mammary stem/progenitor cells. *Breast Cancer*
728 *Res* **2004**;6:R605-15
- 729 45. Aster JC, Pear WS, Blacklow SC. The Varied Roles of Notch in Cancer. *Annu Rev Pathol*
730 **2017**;12:245-75
- 731 46. Zhou B, Lin W, Long Y, Yang Y, Zhang H, Wu K, *et al.* Notch signaling pathway: architecture,
732 disease, and therapeutics. *Signal Transduct Target Ther* **2022**;7:95
- 733 47. Kelliher MA, Roderick JE. NOTCH Signaling in T-Cell-Mediated Anti-Tumor Immunity and T-Cell-
734 Based Immunotherapies. *Front Immunol* **2018**;9:1718
- 735 48. Vera L, Garcia-Olloqui P, Petri E, Vinado AC, Valera PS, Blasco-Iturri Z, *et al.* Notch3 Deficiency
736 Attenuates Pulmonary Fibrosis and Impedes Lung-Function Decline. *Am J Respir Cell Mol Biol*
737 **2021**;64:465-76
- 738 49. Sun H, Liu F, Lin Z, Jiang Z, Wen X, Xu J, *et al.* Silencing of NOTCH3 Signaling in Meniscus Smooth
739 Muscle Cells Inhibits Fibrosis and Exacerbates Degeneration in a HEYL-Dependent Manner. *Adv*
740 *Sci (Weinh)* **2023**;10:e2207020

741

742 **Figure Legend**743 **Figure 1:**

- 744 (A) Overview of the study design and analytical framework.
 745 (B) Uniform manifold approximation and projection (UMAP) of cells from 9 donors colored by cell
 746 types. Top right: cells in adjacent non-tumor (ANT) tissues; Bottom right: cells in tumors (T).
 747 Annotations for each cluster were identified by canonical markers.
 748 (C) Dot plot of the average expression of selected canonical markers used for cluster annotation.

749 **Figure 2:**

- 750 (A) UMAPs of mesenchymal cells colored by subclusters. CAF, cancer associated fibroblasts; LRF,
 751 lung resident fibroblasts; SMC, smooth muscle cells.
 752 (B) UMAPs color-coded by the relative expression of marker genes used for subcluster annotation.
 753 (C) Boxplot visualizing the relative fractions of each mesenchymal subcluster to all mesenchymal
 754 populations in T (red) and ANT (blue). The statistical significance was determined using a
 755 Wilcoxon rank-sum test.
 756 (D) Representative flow cytometry plots of EPCAM⁻, CD45⁻, CD31⁻ mesenchymal cells from the
 757 MRC008 tumor stained for FAP and MCAM (top) and FAP and PDPN (bottom).
 758 (E) Heatmap visualizing the relative expression of differentially expressed genes among the four
 759 mesenchymal subtypes. Expression of each gene was normalized by rows. Columns were
 760 grouped by cluster annotation of each cell.
 761 (F) Heatmap visualizing the correlation between the average expression of mesenchymal subset
 762 fingerprints (columns) and expression of canonical marker genes or established signatures
 763 (rows) in the LUAD samples of the Collaboration dataset.
 764 (G) Violin plots visualizing the differential expression of CAF subset fingerprints among the four
 765 mesenchymal subtypes. Left: inflammatory CAFs (iCAFs); right: myofibroblastic CAFs (myCAF).

766 **Figure 3:**

- 767 (A) Representative images of the hematoxylin and eosin (H&E), TTF-1 and p63 IHC staining of an
 768 LSCC sample. Scale bar, 100 μ m. One H&E was done per tumor cross section.
 769 (B) Representative IMC images of a LUAD sample stained with indicated antibodies. Scale bar, 100
 770 μ m
 771 (C) IMC image with a cell segmentation mask as indicated by cell segmentation lines.
 772 (D) Cell phenotypes from 7 LUAD samples shown in the heat map were determined by normalized
 773 median epitome expression of stained antibodies.
 774 (E) Waterfall plots showing the percentage of images, in which each cluster significantly interacts or
 775 avoids interactions with cluster 8, 7, or 16. Significance was determined by a permutation test (p
 776 < 0.01). Numbers on top of each bar indicate the exact value of percentage of significant images.

777 **Figure 4:**

- 778 (A) (left) UMAP highlighting Lymphatic ECs and Vascular ECs. (middle) Vascular ECs colored by cell
 779 subclusters. Top right: cells in ANT tissues; Bottom right: cells in T tissues.

- 780 (B) Boxplot visualizing the relative fractions of each endothelial subcluster to all Vascular EC
 781 populations in T (red) and ANT (blue). The statistical significance was calculated using a
 782 Wilcoxon rank-sum test.
- 783 (C) The average expression of marker genes used for EC subcluster labeling.
- 784 (D) Bar chart visualizing significant cell-cell contact signaling pathways between mesenchymal cells
 785 and ECs generated using CellChat, where the relative strength in T was colored in red and ANT
 786 was in green, and labels were colored in red if the signal was significantly enriched in T
 787 comparing to ANT, or green if significantly enriched in ANT. The pathways are ranked based on
 788 their differences of relative information flow between T and ANT.
- 789 (E) Heatmap visualizing the relative signaling strengths of significant T-enriched pathways in Figure
 790 4d among endothelial and mesenchymal cells generated using CellChat. The top bar plot
 791 represents the total signaling strength of all displayed signaling pathway in each cell group; The
 792 right grey bar plot shows the total signaling strength of all displayed cell groups in each signaling
 793 pathway.
- 794 (F) Chord diagram visualizing the information flow strength of NOTCH signaling pathway from ECs
 795 to mesenchymal cells. The chords were color-coded by the signal senders or receivers of
 796 represented L-R pairs. *NOTCH3* expressed by pericytes shown to be the dominant receptor.
- 797 (G) Forest plot visualizing the significances of NOTCH pathway receptor expression enrichment in
 798 mesenchymal cells among leave-one-donor-out iterations. The Interquartile Range (IQR) of
 799 Benjamini-Hochberg adjusted *p*-values are shown. If there was no significant enrichment
 800 between T and NAT before removing any donors, the data points would be omitted. The red
 801 dash lines represent *p*-value = 0.05.
- 802 (H) Forest plots visualizing the significances of NOTCH pathway ligands expression enrichment in
 803 ECs among leave-one-donor-out iterations.
- 804 (I) Immunofluorescence imaging of a tumor sample from the scRNA-seq cohort. NOTCH3 staining:
 805 green; MCAM staining: orange; DAPI nuclei staining: blue. Scale bar: 100 μ m; white arrow:
 806 MCAM+NOTCH3+ cells
- 807 (J) Boxplots showing the log₁₀ expression of NOTCH receptor genes between T and ANT LUAD
 808 samples in TCGA. For genes with significantly different expression between T and ANT (Wilcoxon
 809 rank-sum test, Benjamini-Hochberg -adjusted *p*-value<0.05), the receiver operating
 810 characteristic – area under the curve (ROC-AUC) values were calculated and colored in red (T-
 811 enriched) or green (ANT-enriched).
 812

813 **Figure 5:**

- 814 (A) Flow cytometry plots of in-vitro expanded mesenchymal cells from MRC002, 003, and 004 tumor
 815 samples stained with NOTCH3 and MCAM antibodies. Black line: antibody staining; gray line:
 816 fluorescence minus one (FMO) control.
- 817 (B) Relative fold changes of NOTCH pathway downstream targets in DMSO or 1 μ M MRK-003
 818 treated mesenchymal and endothelial cell cocultures. Paired *t*-test was used to calculate *p*-
 819 value.
- 820 (C) Heat map of the Log₂ fold changes of genes encoding extracellular matrix or adhesion molecules
 821 in DMSO or 1 μ M MRK-003 treated mesenchymal and endothelial cell cocultures from 3 donors.
 822 Paired *t*-test was used to calculate *p* value. Red colored genes indicate significant increases or

823 decreases in MRK-003 treated groups in at least 2 donors. Gray indicates undetectable
824 transcripts.

825 (D) The concentration of COL1A1 in supernatants collected from DMSO or 1 μ M MRK003 treated
826 mesenchymal and endothelial cell cocultures.

827 (E) Representative images of mesenchymal cell invasion in DMSO or 10 μ M MRK003 treated
828 groups.

829 (F) Quantification of the largest invading area of mesenchymal cells derived from MRC002, 003, and
830 004 tumor samples in DMSO or 10 μ M MRK003 treated groups over 136 hours. Two-way
831 ANOVA was used to calculate p value.

832 (G) Flow cytometry plot of D4A1 mesenchymal cells stained with a NOTCH3 antibody. Black line:
833 antibody staining; gray line: fluorescence minus one (FMO) control.

834 (H) Quantification of the largest invading area of D4A1 mesenchymal cells in DMSO or 10 μ M
835 MRK003 treated groups over 136 hours. Two-way ANOVA was used to calculate p value.

836 (I) Quantification of integrated red intensity, representing tumor invasion signals, in largest
837 invading areas in DMSO or 10 μ M MRK-003 treated groups over 136 hours in H1299 and D4A1
838 coculture spheroids. Two-way ANOVA was used to calculate p value. At least 3 biological
839 replicates were performed for each experiment. *, $p < 0.05$; **, $p < 0.01$; ***, $p < 0.001$; ****, p
840 < 0.0001 ; n.s., not statistically significant.

841 **Figure 6:**

842 (A) Spearman correlation between global genes and *NOTCH3* expression in the TCGA LUAD tumor
843 dataset (x-axis) and Collaboration LUAD tumor dataset (y-axis). *NOTCH3* and *COL1A1* are
844 highlighted in red. The legend presents the correlation value of gene *COL1A1* with *NOTCH3*
845 expression: 0.50 for TCGA dataset and 0.46 for Collaboration dataset.

846 (B) Dot plots of top 10 pathways enriched in KEGG or GeneGo pathways using genes with *NOTCH3*
847 correlations over 0.4(d). Colors indicate p -values; sizes of the dots indicate overlap gene counts
848 in the pathways.

849 (C-E) Cox Proportional hazards analysis showing the predictivity of NOTCH genes in LUAD samples
850 under different stromal level conditions. Genes with significant predictivities (p -value < 0.05) were
851 color-coded by their HR value: red for poor prognosis and blue for better prognosis. Non-significant
852 genes were shown in black dots.

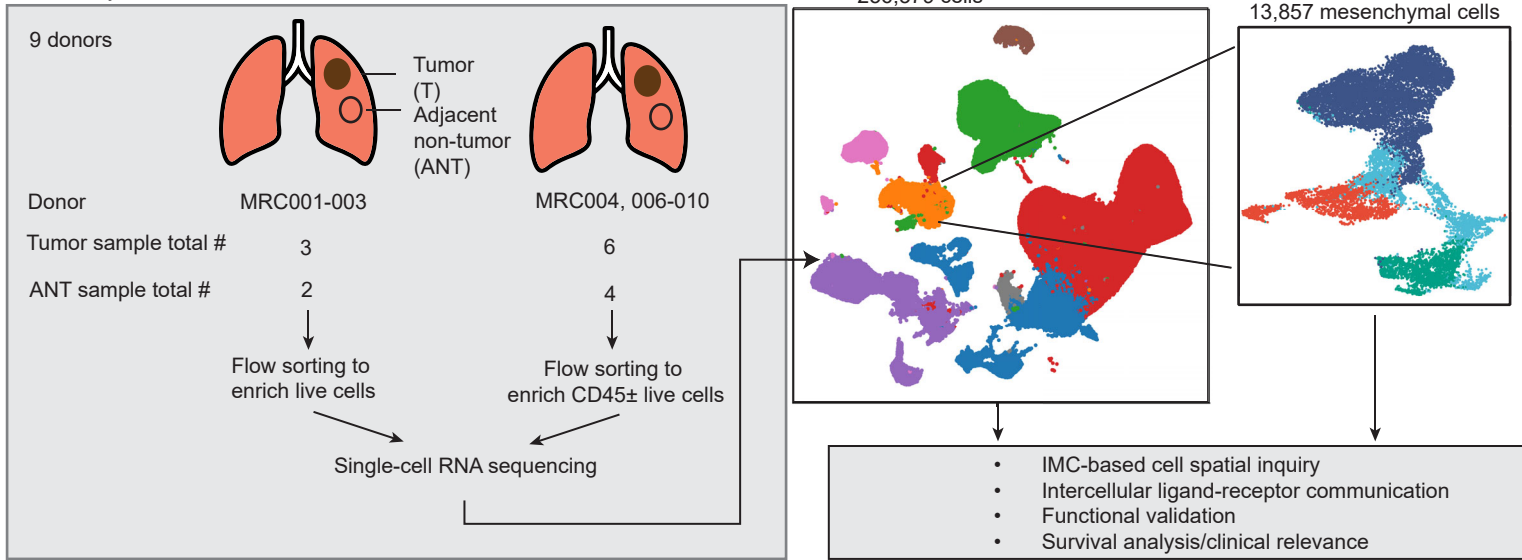
853 (F-G) The Kaplan Meier (KM) Survival Analysis depicting the prognostic value of GEP expression
854 levels in *NOTCH3*- high (F) and *NOTCH3*-low (G) LUAD samples. 1434 LUAD samples with
855 corresponding overall survival (OS) data in the Collaboration dataset were evenly divided into two
856 groups by *NOTCH3* expression level. Hazard ratios were derived from a Cox proportional model fit,
857 no multiple testing. The predictivity of GEP was only sufficient in *NOTCH3*-low samples.

858 (H) Spearman correlation between *NOTCH3* and consensus gene signatures, added to the global
859 gene correlation, in the TCGA LUAD tumor dataset (x-axis) and Collaboration LUAD tumor
860 dataset (y-axis). The legend shows the correlation values, with the first value representing the
861 TCGA dataset and the second value representing the Collaboration dataset.

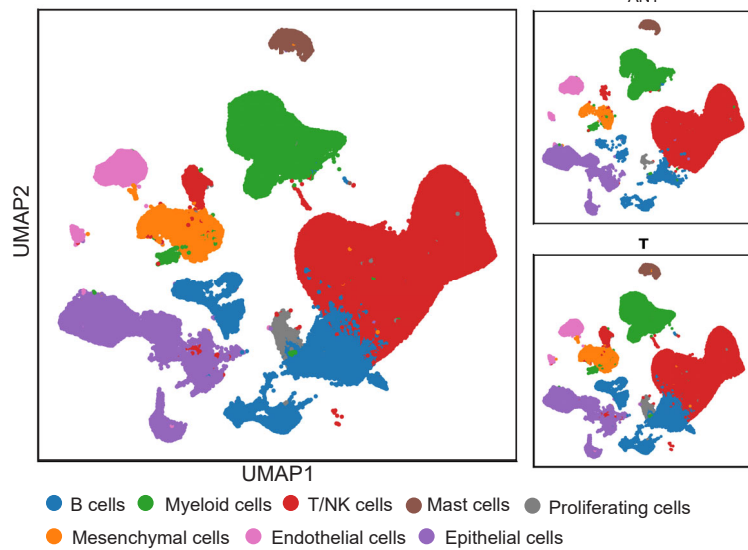
862 (I) Graph illustration of the interaction between mesenchymal and ECs via the NOTCH pathway in
863 the TME. The interaction activates mesenchymal cells and leads to collagen deposition and cell
864 invasion. The graph was created with BioRender.com.

Figure 1.

A. Study schema



B.



C.

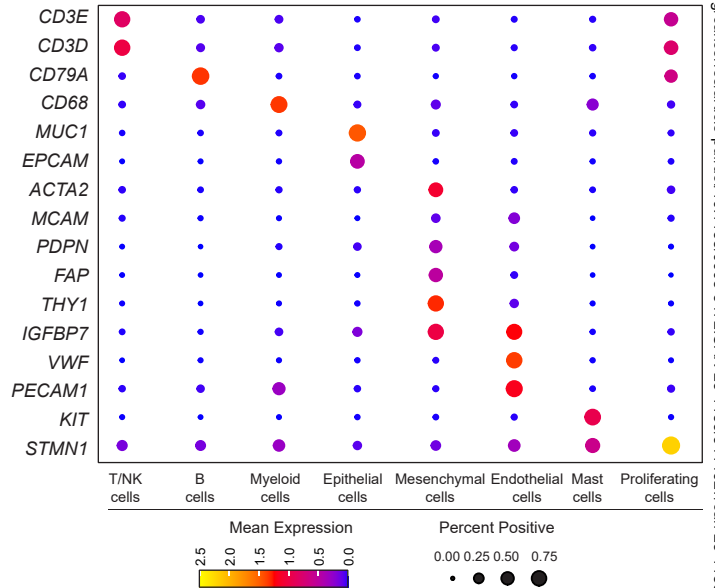


Figure 2.

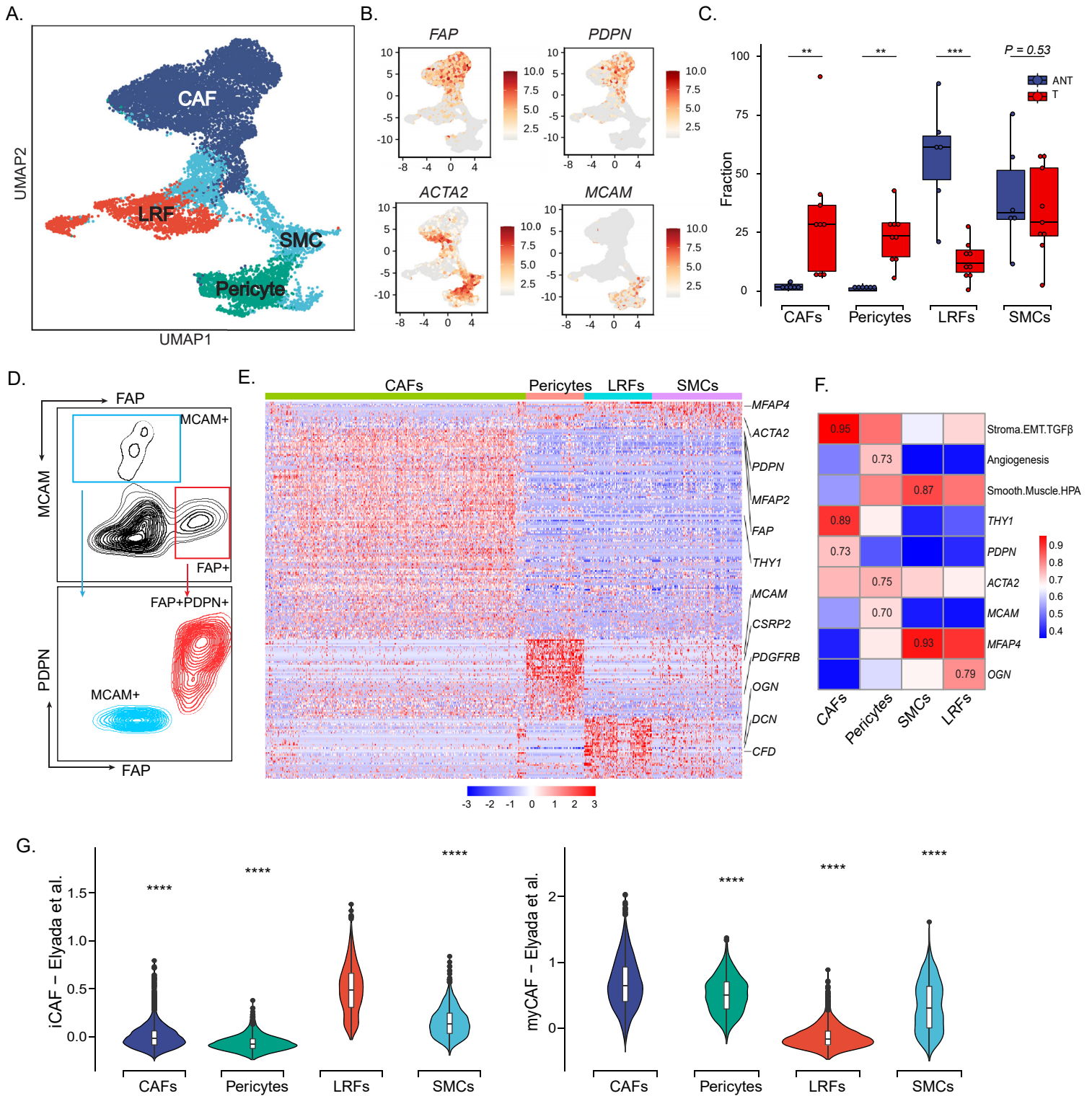


Figure 3.

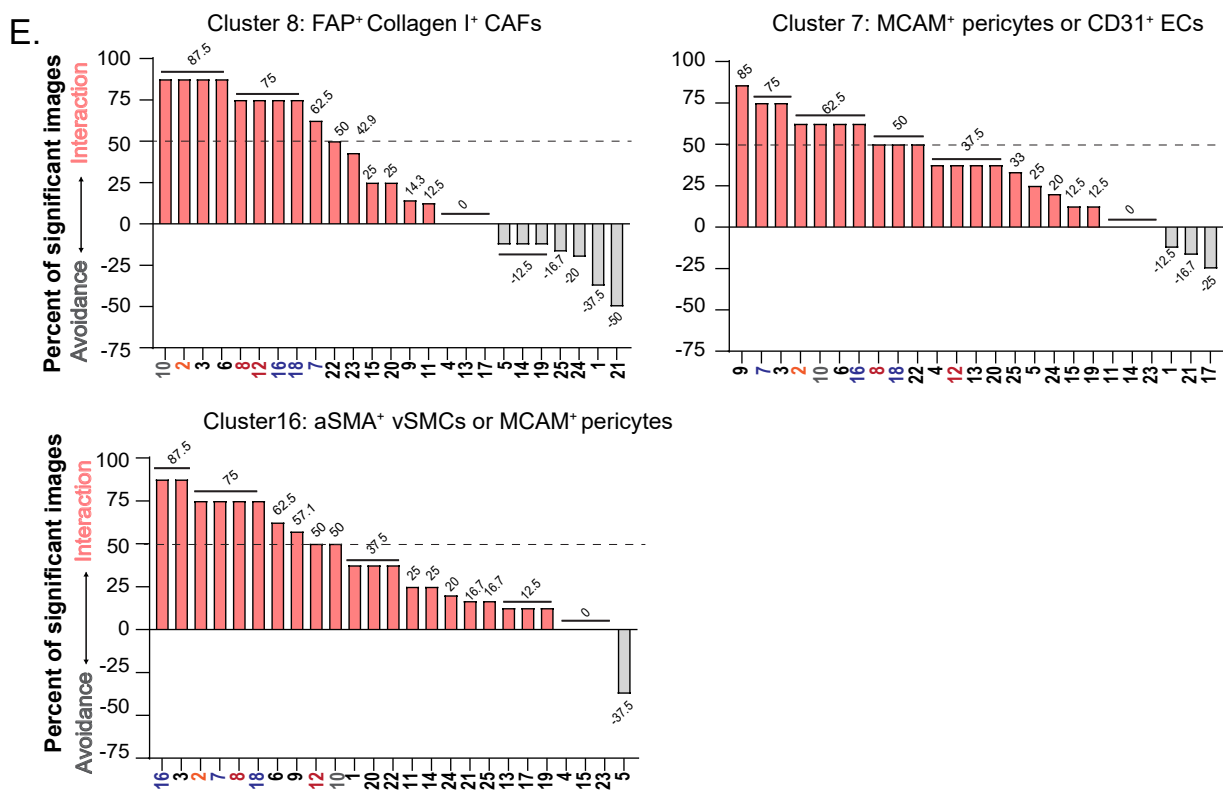
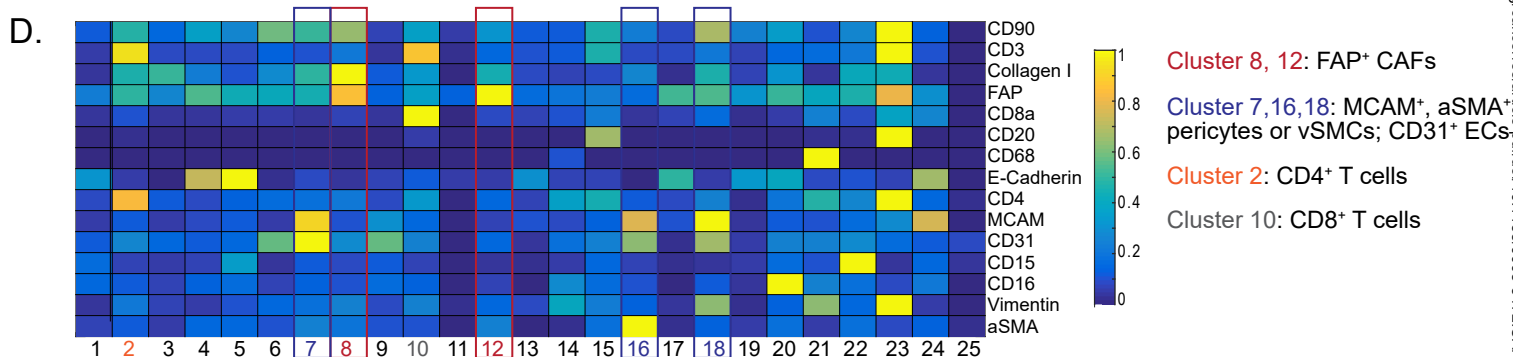
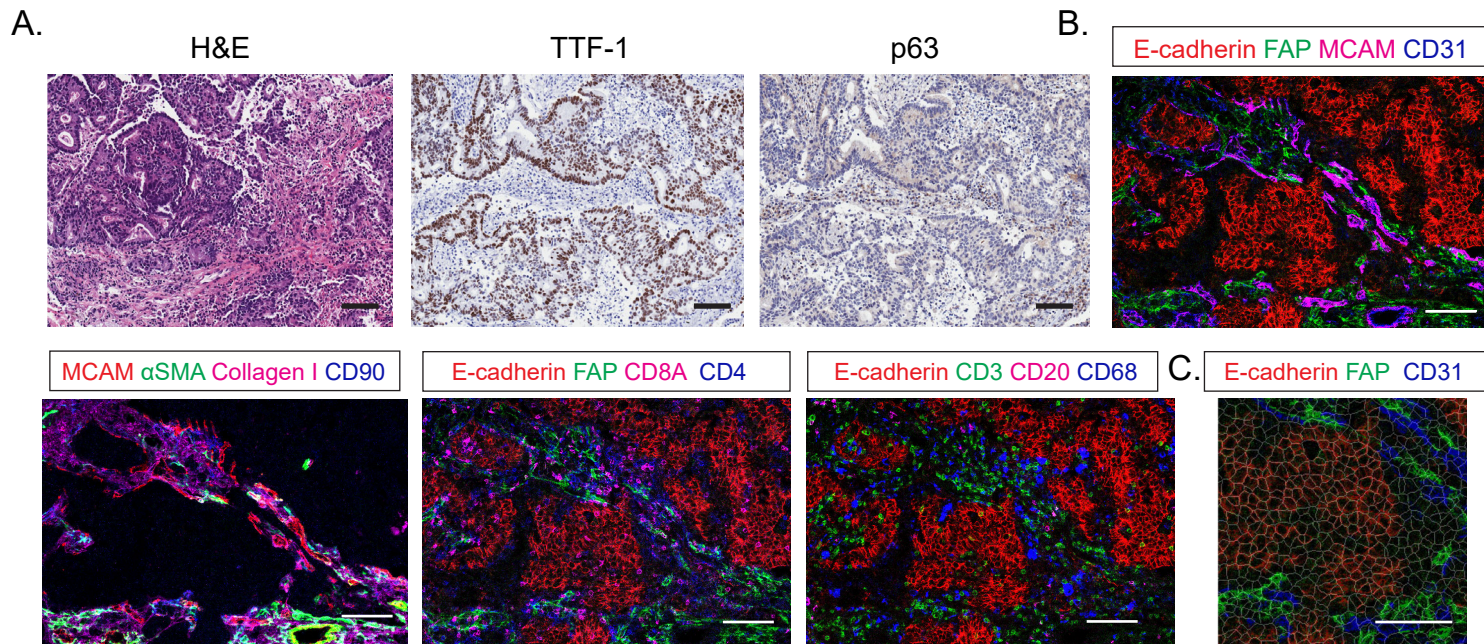


Figure 4.

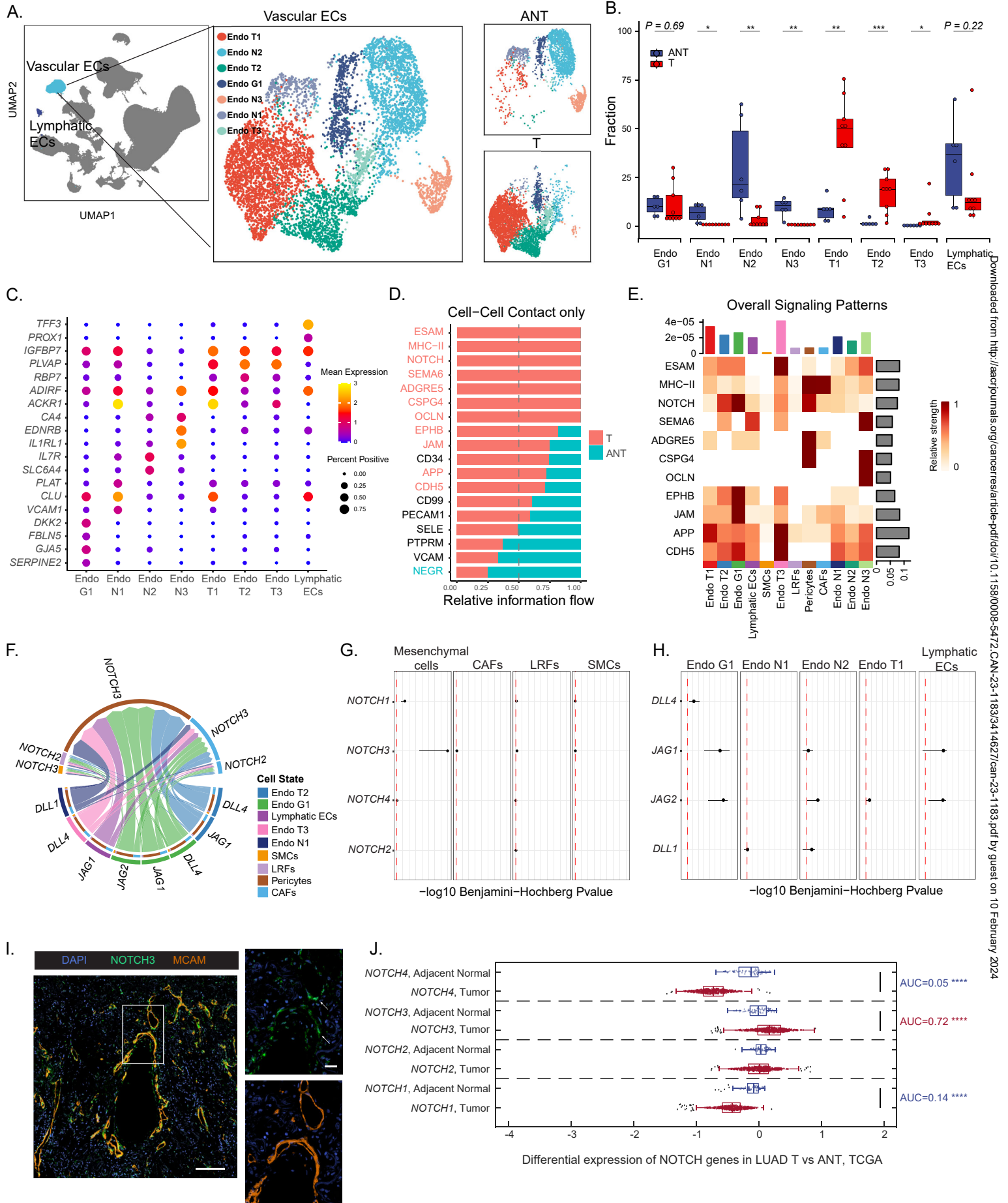


Figure 5.

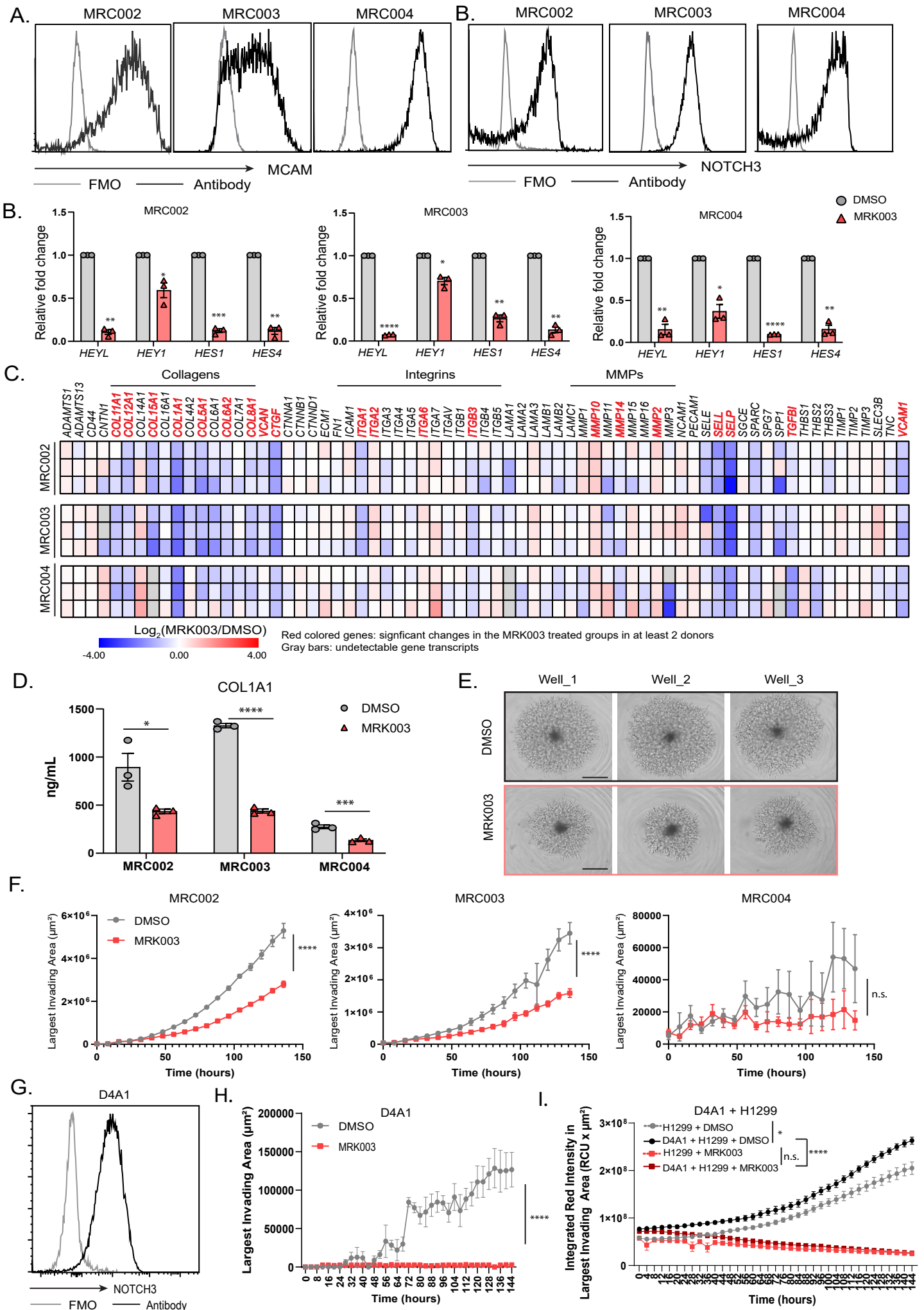


Figure 6.

